
Proximity Matters: Local Proximity Preserved Balancing for Treatment Effect Estimation

Hao Wang¹ Zhichao Chen¹ Yuan Shen¹ Jiajun Fan² Zhaoran Liu¹
Degui Yang⁴ Xinggao Liu¹ Haoxuan Li^{3*}
¹Zhejiang University ²Tsinghua University
³Peking University ⁴Central South University
haohaow@zju.edu.cn

Abstract

Heterogeneous treatment effect (HTE) estimation from observational data poses significant challenges due to treatment selection bias. Existing methods address this bias by minimizing distribution discrepancies between treatment groups in latent space, focusing on global alignment. However, the fruitful aspect of local proximity, where *similar units exhibit similar outcomes*, is often overlooked. In this study, we propose **Proximity-aware Counterfactual Regression (PCR)** to exploit proximity for representation balancing within the HTE estimation context. Specifically, we introduce a local proximity preservation regularizer based on optimal transport to depict the local proximity in discrepancy calculation. Furthermore, to overcome the curse of dimensionality that renders the estimation of discrepancy ineffective—exacerbated by limited data availability for HTE estimation—we develop an informative subspace projector, which trades off minimal distance precision for improved sample complexity. Extensive experiments demonstrate that PCR accurately matches units across different treatment groups, effectively mitigates treatment selection bias, and significantly outperforms competitors. Code is available at <https://anonymous.4open.science/status/ncr-B697>.

1 Introduction

Estimating HTE through randomized controlled trials is fundamental in causal inference, widely applied in various domains such as healthcare [48], e-commerce [1, 30, 62], and education [8]. While randomized controlled trials are considered the gold standard in HTE estimation [26, 41], their practical deployment is often limited by significant financial and ethical constraints [25, 60]. Consequently, there is increasing reliance on observational data to estimate HTE, prompted by the broader accessibility of such data and the feasibility of conducting post-marketing surveillance instead of costly clinical trials [28, 61, 66].

HTE estimation from observational data presents significant challenges primarily due to: (1) the absence of counterfactuals, where only one out of all potential outcomes is observable, and (2) the presence of treatment selection bias, where non-random treatment assignments lead to a covariate shift between treated and untreated groups, affecting the generalizability of outcome estimators across the population [59, 60]. Traditional meta-learners address the missing counterfactuals by segmenting the HTE estimation into more manageable tasks focused on factual outcomes [22]. Nevertheless, these approaches often struggle with the covariate shift, resulting in biased HTE estimations.

Recent methods such as counterfactual regression have demonstrated promise by mitigating selection bias through minimizing distribution discrepancies in the representation space [6, 17, 49, 67, 68].

*Corresponding author.

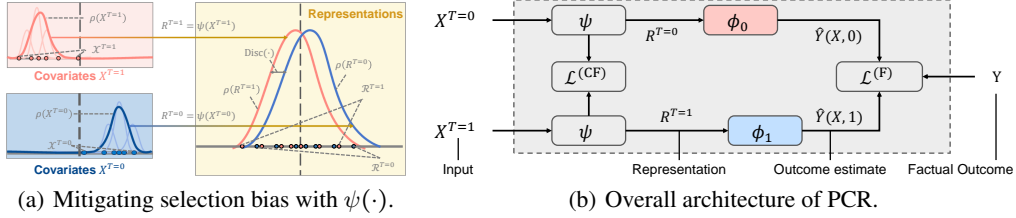


Figure 1: Overview of handling treatment selection bias with PCR. The red and blue colors signify the treated and untreated groups, respectively. (a) The treatment selection bias is illustrated through a distribution shift between treated (X_1) and untreated (X_0) units. The curves and scatters indicate the probability density functions and associated empirical distributions, respectively. (b) PCR reduces selection bias by aligning units from both treatment groups within a common representation space, denoted as $R = \psi(X)$. This alignment facilitates the generalization of the outcome mappings ϕ_1 and ϕ_0 across different groups.

Despite their efficacy, these approaches predominantly overlook two critical issues. First, they emphasize a global perspective in calculating distribution discrepancies, neglecting the local proximity between treatment units. Local proximity—where similar units likely exhibit similar outcomes—is a pivotal factor in accurate HTE estimation [10, 46, 55]. Ignoring this aspect can lead to misleading discrepancy estimates and consequently erroneous updates to the HTE estimator. The second challenge pertains to the curse of dimensionality, where a substantial number of units is required to reliably estimate treatment effects. Often, acquiring a sufficiently large sample of treated units is impractical in real-world settings, rendering these discrepancy estimates unreliable. Thus, addressing these overlooked aspects is essential for advancing the precision and applicability of HTE estimations from observational data.

Contributions and outline. In this paper, we propose an effective HTE estimator based on optimal transport, namely Proximity-aware CounterFactual Regression (PCR), which handles both issues above with a generalized optimal transport problem. Specifically, after presenting preliminaries in Section 3.1, we construct a local proximity preservation regularizer within the framework of optimal transport to incorporate local proximity in Section 3.1. We subsequently justify the curse of dimensionality in Section 3.2 and introduce an informative subspace projector (ISP) to handle it. The architecture and learning objectives of PCR are elaborated upon in Section 3.3, followed by the presentation of our experimental results in Section 4.

2 Preliminaries

2.1 Heterogeneous treatment effect estimation with observational data

This section outlines the HTE estimation task within the potential outcome framework [47] and the challenge of treatment selection bias. The fundamental is encapsulated in Definition 2.1². Specifically, a unit characterized by covariates x possesses two potential outcomes: Y_1 if treated and Y_0 if untreated. The expected difference between these potential outcomes given covariates, represented as $\tau(x) = \mathbb{E}[Y_1 - Y_0 \mid x]$, is termed as the conditional average treatment effect (CATE), and its expectation over all units is termed as the average treatment effect (ATE).

Definition 2.1. Suppose X , R , Y , and T are random variables with probability density function ρ_* and support \mathcal{S}_* . Typically, X represents covariates with the probability density function ρ_X and support $\mathcal{S}_X = \{0, 1\}$. R represents induced representations, Y denotes outcomes, and T denotes treatment indicators.

Definition 2.2. Suppose $\psi : \mathcal{S}_X \rightarrow \mathcal{S}_R$ is a representation mapping with $R = \psi(X)$. Define $\phi_T : \mathcal{R} \times \mathcal{T} \rightarrow \mathcal{Y}$ as an outcome mapping that maps the representations and treatment to the corresponding factual outcome: $Y_1 = \phi_1(R)$ and $Y_0 = \phi_0(R)$.

²We use uppercase letters, e.g., X , to denote a random variable, and lowercase letters, e.g., x , to denote a specific value. Letters in calligraphic font, e.g., \mathcal{X} , represent the empirical distribution, and $\mathbb{P}(\cdot)$ represents the probability distribution function, e.g., $\mathbb{P}(X)$.

Definition 2.3. Suppose \mathcal{X} , \mathcal{R} , and \mathcal{Y} are the empirical distributions of X , R , and Y at a minibatch level, respectively. Let $\mathcal{X}^{T=1}$ and $\mathcal{X}^{T=0}$ be the covariates of treated and untreated units, respectively, with $\mathcal{R}_{\psi}^{T=1}$ and $\mathcal{R}_{\psi}^{T=0}$ as the corresponding representations induced by $R = \psi(X)$.

Therefore, estimation of CATE is the cornerstone in HTE estimation. Since one of these outcomes is always unobserved in a dataset, effective CATE estimation typically involves decomposing it into factual outcome estimation subproblems solvable with supervised regression methods [22]. An exemplary approach TARNet [49] employs the representation mapping ψ and outcome mapping ϕ from Definition 2.2, which estimates the CATE as

$$\hat{\tau}_{\psi, \phi}(x) = \hat{Y}(x, 1) - \hat{Y}(x, 0), \quad \hat{Y}(x, 1) = \phi_1(\psi(x)), \quad \hat{Y}(x, 0) = \phi_0(\psi(x)), \quad (1)$$

where ψ is trained across all units, while ϕ_1 and ϕ_0 are trained separately on treated and untreated groups. The training objective is to minimize the factual outcome estimation error:

$$\mathcal{L}^{(F)}(\psi, \phi) := \sum_{i=1}^N \|\phi_1(\mathcal{R}_{\psi, i}^{T=1}) - \mathcal{Y}_i^{T=1}\|_2^2 + \sum_{j=1}^M \|\phi_0(\mathcal{R}_{\psi, j}^{T=0}) - \mathcal{Y}_j^{T=0}\|_2^2 \quad (2)$$

where \mathcal{R}_{ψ} and \mathcal{Y} are the empirical distributions of representations and outcomes as defined in Definition 2.3, and i and j are sample indices in the associated empirical distribution. CATE estimators are evaluated using the precision in estimation of heterogeneous effect (PEHE) metric:

$$\epsilon_{\text{PEHE}}(\psi, \phi) := \int (\hat{\tau}_{\psi, \phi}(x) - \tau(x))^2 \rho(x) dx. \quad (3)$$

Selection bias. As illustrated in Figure 1(a), treatment selection bias introduces a distribution shift of covariates between groups, which causes ϕ_1 and ϕ_0 to overfit to their respective group’s characteristics and generalize poorly across the entire population. To mitigate selection bias, seminal works starting from CFR [49] augment the learning objective with a *distribution discrepancy* term as $\mathcal{L}^{(F)} + \text{Disc}(\mathcal{R}_{\psi}^{T=1}, \mathcal{R}_{\psi}^{T=0})$. This adjustment reduces distribution shift in the representation space, thereby enabling ϕ_1 and ϕ_0 to generalize to both treated and untreated groups.

2.2 Local proximity for HTE estimation

Local proximity, quantified as the mutual distance between units within a distribution, captures the geometric properties of distributions. The assumption that *similar units have similar outcomes* [67, 68] highlights the importance of local proximity for HTE estimation. This is evidenced by the success of HTE estimators based on matching (KNN [10], PSM [46]) and stratification [55].

Despite the recognized significance of local proximity, state-of-the-art representation-based estimators, predominantly following the CFR [49, 57] paradigm, primarily focus on global alignment by minimizing global discrepancy $\text{Disc}(\cdot)$. These methods often neglects local proximity [50], which is crucial for accurate HTE estimation. A notable exception is the SITE model [67], which employs the PDDM and MPDM metrics [18] to depict local proximity and global discrepancy, respectively. However, both metrics are computed using only six selected anchor units [68], ignoring the role of other units and resulting in suboptimal performance due to insufficient granularity of the analysis.

Our work builds upon the idea of exploiting local proximity in SITE, and proposes a more comprehensive approach that moves beyond specific anchor units, to model both local proximity and global discrepancy in a unified framework, leveraging the optimal transport methodology.

2.3 Discrete optimal transport and Sinkhorn divergence

Optimal transport (OT) quantifies distribution discrepancy as the minimum transport cost, offering a tool to quantify the treatment selection bias in Figure 1(a). An applicable formulation proposed by Kantorovich [20] is present in Definition 2.4, which can be seen as a linear programming problem.

Definition 2.4. For empirical distributions α and β with n and m units, respectively, the Kantorovich problem aims to find a feasible plan $\pi \in \mathbb{R}_+^{n \times m}$ which transports α to β at the minimum cost:

$$\mathbb{W}(\alpha, \beta) := \min_{\pi \in \Pi(\alpha, \beta)} \langle \mathbf{D}, \boldsymbol{\pi} \rangle, \quad \Pi(\alpha, \beta) := \{ \boldsymbol{\pi} \in \mathbb{R}_+^{n \times m} : \boldsymbol{\pi} \mathbf{1}_m = \mathbf{a}, \boldsymbol{\pi}^T \mathbf{1}_n = \mathbf{b} \}, \quad (4)$$

where $\mathbb{W}(\alpha, \beta) \in \mathbb{R}$ is the OT discrepancy between α and β ; $\mathbf{D} \in \mathbb{R}_+^{n \times m}$ is the unit-wise distance between α and β , which is implemented with the Euclidean distance; \mathbf{a} and \mathbf{b} are the mass of units in α and β , and Π is the feasible plan set where the mass-preserving constraint holds.

Since exact solutions to (4) often come with high computational costs [2], researchers would advocate adding an entropic regularization to the Kantorovich problem which makes the problem ϵ -convex and solvable with the Sinkhorn algorithm [11]. The Sinkhorn algorithm only consists of matrix-vector products, making it suited to be accelerated with GPUs.

3 Proposed method

In this section, we present the Proximity-aware Counterfactual Regression (PCR) approach, which leverages optimal transport to tackle the treatment selection bias. We first illustrate local proximity preservation regularizer (LPR) based on optimal transport framework for measuring and maintaining local similarities in different treatment groups, and demonstrate its efficacy for improving HTE estimation. Subsequently, we propose an informative subspace projector (ISP) to reduce the sampling complexity and handle the curse of dimensionality. We finally open a new thread to summarize the model architecture, learning objectives, and optimization algorithm.

3.1 Local proximity preservation regularizer for counterfactual regression

To mitigate treatment selection bias, representation-based methods align treated and untreated groups in the representation space, the core of which is the quantification of the distribution discrepancy $\text{Disc}(\cdot)$ between treatment groups. It is plausible to quantify the discrepancy with OT due to its numerical advantages and flexibility over competitors [57]. However, standard OT fails to preserve local proximity, a crucial aspect in HTE estimation. The treated and untreated units with similar neighbors for instance should have a higher probability of matching together since similar units have similar outcomes [46, 55]. An extension of OT that encodes local proximity is the Gromov-Wasserstein measure, primarily applied to matching objects with geometric structures [37, 63]. Resonating with [53], the LPR fuses the Gromov Wasserstein measure and restates the transport problem in the representation space as:

$$\mathbb{F}(\mathcal{R}_{\psi}^{T=0}, \mathcal{R}_{\psi}^{T=1}) := \min_{\pi \in \Pi(\alpha, \beta)} \left(\kappa \cdot \langle \pi, \mathbf{D} \rangle + (1 - \kappa) \cdot \sum_{i,j,k,l} \mathbf{P}_{i,j,k,l} \pi_{i,j} \pi_{k,l} \right). \quad (5)$$

The above optimization problem consists of two components with relative strengths controlled by κ . The first term, adhering to the standard OT formulation in (4), measures the global discrepancy with $\mathbf{D}_{i,j} = \|\mathcal{R}_{\psi,i}^{T=0} - \mathcal{R}_{\psi,j}^{T=1}\|_2^2$. The second term depicts local proximity within each treatment group as $\mathbf{D}_{i,j}^t = \|\mathcal{R}_{\psi,i}^{T=t} - \mathcal{R}_{\psi,j}^{T=t}\|_2^2$, and preserve such local proximity via $\mathbf{P}_{i,j,k,l} = \|\mathbf{D}_{i,k}^{T=0} - \mathbf{D}_{j,l}^{T=1}\|_2$. Specifically, if the distance between $\mathcal{R}_{\psi,i}^{T=0}$ and $\mathcal{R}_{\psi,k}^{T=0}$ is close to that between $\mathcal{R}_{\psi,j}^{T=1}$ and $\mathcal{R}_{\psi,l}^{T=1}$ (i.e., $\|\mathbf{D}_{i,k}^{T=0} - \mathbf{D}_{j,l}^{T=1}\|_2 \rightarrow 0$), a higher volume of mass will be matched, indicated by a larger $\pi_{i,j} \pi_{k,l}$. Conversely, if there is a significant disparity, less mass will be transported. The derived transport plan encourages matching units with similar neighbors, preserving local proximity. Therefore, \mathbb{F} quantifies the discrepancy between treatment groups while accommodating the local similarities.

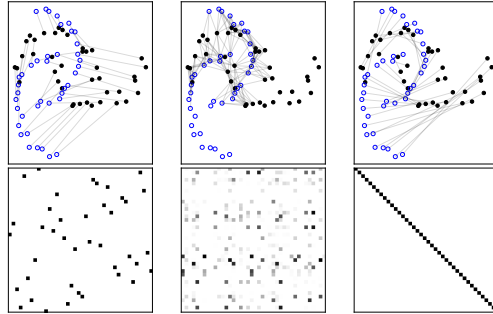


Figure 2: The transport strategy (upper) and corresponding matrix visualization (down) in three HTE estimators: CFR [49] (left), ES-CFR [57] (center) and Ours (right). Different scatter colors indicate different treatments.

Figure 2 provides a toy example that illustrates the significance of local proximity preservation in aligning different treatment groups. The example contrasts several approaches to handling the inherent discrepancies between treated and untreated groups. The canonical Wasserstein discrepancy in CFR [49] aims for global alignment between groups. However, it often leads to erroneous matchings as it does not account for local similarities, resulting in mismatches that can mislead the update of HTE estimators. The unbalanced Wasserstein discrepancy in ESCFR [49] discards skewed samples

and concentrates on aligning units that overlap between treatment groups. Despite improvements, this strategy can still produce a noisy and blurred transportation of units. Our methodology integrates LPR to exploit local similarities effectively, refining the transportation strategy and ensuring precise matching of all samples. This precision is vital for training HTE estimator, as it generates accurate gradient signals for updating representation mappings.

The utility of the local-similarity preserved discrepancy for regularizing HTE estimators is investigated by Theorem 3.1 (refer to Appendix A.4 for proof), which demonstrates that the PEHE can be optimized by minimizing the estimation error of factual outcomes and the group discrepancy.

Theorem 3.1. *Let ψ and ϕ be the representation mapping and factual outcome mapping, respectively; $\hat{\mathbb{W}}_\psi$ be the group discrepancy at a mini-batch level. With the probability of at least $1 - \delta$, we have:*

$$\epsilon_{\text{PEHE}}(\psi, \phi) \leq 2[\epsilon_{\text{F}}^{T=1}(\psi, \phi) + \epsilon_{\text{F}}^{T=0}(\psi, \phi) + B_{\psi, \kappa} \mathbb{F}(\mathcal{R}_\psi^{T=0}, \mathcal{R}_\psi^{T=1}) - 2\sigma_Y^2 + \mathcal{O}(N^{-\frac{2}{d}})], \quad (6)$$

where $\epsilon_{\text{F}}^{T=1}$ and $\epsilon_{\text{F}}^{T=0}$ are the expected errors of factual outcome estimation, N is the batch size, σ_Y^2 is the variance of outcomes, $B_{\psi, \kappa}$ is a constant term, and $\mathcal{O}(\cdot)$ is a sampling complexity term.

3.2 Informative subspace projector for the curse of dimensionality

The curse of dimensionality refers to the phenomenon where the Euclidean distance between data points tend to be identical [15]. It renders Euclidean distance difficult to model the proximity in high dimensional settings due to diminished discrimination.

From a computational view, the diminishing discrimination necessitates more samples for estimating Euclidean-based discrepancy [36], which is a pivotal component in state-of-the-art HTE estimators such as MMD in [49], PDDM in [67], and EMD in [57]. A well-known result states, for instance, that the sample complexity of EMD can grow exponentially with dimension [7]. Similarly, the sample complexity of \mathbb{F} reaches $\mathcal{O}(N^{-\frac{2}{d}})$, forming the complexity term in Theorem 3.1. Such large sample complexity necessitates many treated and untreated units to faithfully estimate the true discrepancy. However, a large number of treated units is often difficult to acquire in real-world experiments, underscoring the adverse impact of the curse of dimensionality on HTE estimation.

To counteract the curse of dimensionality, reducing the computational space dimension is a common approach. Consider using a projector $U \in \mathbb{R}^{d \times k}$ to transform the data from a high-dimensional space d to a lower-dimensional subspace k . The distance between two unit representations \mathcal{R}_1 and \mathcal{R}_2 in this reduced space is computed as $\|\mathcal{R}_1 U - \mathcal{R}_2 U\|$. This approach alleviates the curse of dimensionality but introduces the risk of losing significant information, potentially leading to overly optimistic discrepancy estimations.

To address the potential pitfalls of naive dimension reduction, it is crucial to choose a projection that maximizes the relevant discrepancy, mitigating the bias induced by dimension reduction. The projection robust optimization formulation is proposed as follows:

$$\mathbb{F}^{(\text{PR})}(\mathcal{R}_\psi^{T=0}, \mathcal{R}_\psi^{T=1}) := \min_{\pi \in \Pi(\mathcal{R}_\psi^{T=0}, \mathcal{R}_\psi^{T=1})} \max_{UU^\top = I} \left(\kappa \cdot \langle \pi, \mathbf{D}^U \rangle + (1 - \kappa) \cdot \sum_{i,j,k,l} \mathbf{P}_{i,j,k,l}^U \pi_{i,j} \pi_{k,l} \right). \quad (7)$$

where $\mathbf{D}_{i,j}^U = \|\mathcal{R}_{\psi,i}^{T=0} U - \mathcal{R}_{\psi,j}^{T=1} U\|_2^2$ is the distance in the reduced k -dimensional space, $P_{i,j,k,l}^U = \|\mathbf{D}_{i,k}^{U,T=0} - \mathbf{D}_{j,l}^{U,T=1}\|_2$. However, this optimization problem proves difficult to solve [36]. An effective compromise involves projecting the data into a k -dimensional subspace through an ISP module that maximally preserves the information, and then compute discrepancy in the subspace. Built upon this idea, the transport problem modified with the ISP module is formulated in Definition 3.1.

Definition 3.1. *Suppose $U^* \in \mathbb{R}^{d \times k}$ an informative subspace projector, such that:*

$$U^* = \arg \min_{U, UU^\top = I} \|\mathcal{R} - RUU^\top\|_2^2, \quad (8)$$

where $P = k/d$ denotes the ratio of dimensionality reduction. The distribution discrepancy equipped with LPR and ISP modules is formulated as

$$\mathbb{F}_{\kappa, P}^{(\text{PCR})}(\mathcal{R}_\psi^{T=0}, \mathcal{R}_\psi^{T=1}) := \min_{\pi \in \Pi(\mathcal{R}_\psi^{T=0}, \mathcal{R}_\psi^{T=1})} \left(\kappa \cdot \langle \pi, \mathbf{D}^{U^*} \rangle + (1 - \kappa) \cdot \sum_{i,j,k,l} \mathbf{P}_{i,j,k,l}^{U^*} \pi_{i,j} \pi_{k,l} \right). \quad (9)$$

3.3 Workflow of proximity-aware counterfactual regression

The architecture of PCR is presented in Figure 1(b), where the covariate X is first mapped to the representations R with $\psi(\cdot)$, and then to the potential outcomes with $\phi(\cdot)$. The learning objective is to minimize the risk of factual outcome estimation and the group discrepancy. Given mini-batch distributions $\mathcal{X}^{T=1}$ and $\mathcal{X}^{T=0}$, the risk of factual outcome estimation can be estimated as (2). Afterwards, the group discrepancy is calculated as $\text{Disc}_{\kappa, P}(\psi) = \mathbb{F}_{\kappa, P}^{(\text{PCR})}(\mathcal{R}_{\psi}^{T=0}, \mathcal{R}_{\psi}^{T=1})$. Finally, the overall learning objective of PCR is

$$\mathcal{L}_{\lambda, \kappa, P}^{(\text{PCR})} := \mathcal{L}^{(\text{F})}(\psi, \phi) + \text{Disc}_{\kappa, P}(\psi), \quad (10)$$

where λ controls the strength of distribution alignment, κ controls LPR in (7), and P controls the ratio of dimension reduction in Definition 3.1. The learning objective above mitigates the selection bias following Theorem 3.1 while handling the issues of local proximity and curse of dimensionality.

The optimization procedure of PCR consists of three steps. First, compute U^* by solving the dimension reduction problem in (8), which can be solved via the well-established principal component analysis algorithm. Second, compute $\mathbb{F}^{(\text{PCR})}$ by solving the OT problem in Definition 3.1 with Algorithm 2, where the projection matrix is U^* . Finally, calculate the overall loss in (10) and update ψ and ϕ with stochastic gradient methods.

4 Experiments

4.1 Experimental setup

Datasets. The evaluation of PEHE is challenged by the absence of counterfactuals in observational data. To address this, experiments are conducted using two semi-synthetic benchmarks [49, 67], namely the Infant Health and Development Program (IHDP) and the Atlantic Causal Inference Conference (ACIC) competition data. The IHDP dataset is constructed to evaluate the effect of specialist home visits on infants’ cognitive development, containing 747 observations with 25 covariates. The ACIC data, derived from the collaborative perinatal project [40], comprises 4802 observations and 58 covariates.

Baselines. The involved baseline methods can be categorized into three groups:

- **Statistical estimators:** random forest with treatment as a covariate (R.Forest), a single neural network model treating the treatment indicator as a covariate (S.learner [22]), separate neural regressors for each treatment group (T.learner [22]), and TARNet [49].
- **Matching estimators:** propensity score matching with logistic regression (PSM [46]), k-nearest neighbor matching (k-NN [10]), and orthogonal forest (O.Forest [55]).
- **Representation-based estimators:** counterfactual regression with Maximum Mean Discrepancy (CFR-MMD), Wasserstein distance (CFR-WASS) [49], and generalized Wasserstein discrepancy (ESCFR) [57]; similarity-preserved individual treatment estimator (SITE) and the recent deep entire space cross network (DESCN) [74].

Training protocol. PCR is implemented with a fully connected neural network architecture comprising two hidden layers with 16-16 and 32-32 nodes, respectively. It is trained using the Adam optimizer for a maximum of 400 epochs, with an early stopping patience set to 30 epochs. The learning rate and weight decay parameters are set at $1e^{-3}$ and $1e^{-4}$, respectively. Other optimization settings follow Kingma and Ba [21]. Hyper-parameters are tuned within the ranges in Section 4.4, with model performance validation conducted every epoch.

Evaluation protocol. We select PEHE (ϵ_{PEHE}), absolute estimation error of ATE (ϵ_{ATE}) and ATT (ϵ_{ATT}) for evaluation. While PEHE is the primary metric for assessing performance [49, 67], it cannot be directly utilized during the model selection phase due to the absence of counterfactual outcomes. Instead, the area under the uplift curve (AUUC) [1] is employed to guide model selection. AUUC assesses the ranking performance of the HTE estimator and can be computed without access to counterfactuals. Although not a standard measure in HTE estimation, AUUC provides valuable insights as an auxiliary metric. Results are reported for both within-sample (training) and out-of-sample (test) datasets, consistent with common practices in the field [33, 34, 49, 67].

Table 1: Out-of-sample performance (mean \pm std) on the ACIC and IHDP datasets. “*” marks the baseline estimators that PCR outperforms significantly at p-value < 0.05 over paired samples t-test.

Dataset	ACIC			IHDP		
	ϵ_{PEHE}	ϵ_{ATE}	ϵ_{ATT}	ϵ_{PEHE}	ϵ_{ATE}	ϵ_{ATT}
R.Forest	3.3908 \pm 0.1811*	0.8347 \pm 0.3635	0.7785 \pm 0.3816	4.6697 \pm 9.2920	0.4544 \pm 0.8308	0.8353 \pm 1.2413
S.Learner	4.8835 \pm 0.7933*	3.0913 \pm 0.7731*	3.1213 \pm 0.6372*	4.7408 \pm 3.9688*	2.5785 \pm 1.8521*	2.7951 \pm 1.6036*
T.Learner	4.2749 \pm 0.6793*	2.2176 \pm 1.2131*	2.3940 \pm 1.1964*	2.5257 \pm 3.3643*	0.5818 \pm 1.2177	0.6642 \pm 1.2197
TARNet	3.5331 \pm 0.9556*	1.5308 \pm 1.0469*	1.6601 \pm 1.0670*	1.7781 \pm 3.4467	0.2814 \pm 0.3193	0.3338 \pm 0.3349
k-NN	5.8977 \pm 0.1400*	1.5773 \pm 0.3075*	1.9068 \pm 0.2870*	4.3191 \pm 7.3361	0.8316 \pm 1.6911	1.8118 \pm 3.2342
O.Forest	2.7451 \pm 0.3379*	0.6003 \pm 0.1879	0.6597 \pm 0.2013	3.1888 \pm 5.6657	0.3150 \pm 0.3696	0.6539 \pm 0.5370*
PSM	5.1014 \pm 0.2987*	0.6468 \pm 0.3478	0.6231 \pm 0.3465	4.6347 \pm 8.5748	0.2129 \pm 0.3362	0.9353 \pm 2.7094
CFR-MMD	3.8514 \pm 0.4558*	1.7379 \pm 0.9133*	1.9060 \pm 0.9290*	1.9398 \pm 2.9029	0.587 \pm 1.2231	0.6678 \pm 1.2207
CFR-WASS	3.3187 \pm 0.7622*	1.3581 \pm 1.0325*	1.4682 \pm 1.0636*	1.9252 \pm 2.9323	0.5578 \pm 1.2455	0.6532 \pm 1.2544
SITE	3.4910 \pm 0.7799*	1.3425 \pm 1.1929	1.5443 \pm 1.2128*	1.7339 \pm 3.1709	0.2271 \pm 0.3140	0.2525 \pm 0.2805
DESCN	2.6420 \pm 0.2614*	0.4548 \pm 0.1693	0.4987 \pm 0.1881	4.0128 \pm 6.1409*	1.2219 \pm 1.7453	0.7917 \pm 1.3185
ESCFR	2.6780 \pm 0.6566	1.1468 \pm 0.8146*	1.2365 \pm 0.8689*	1.6299 \pm 3.0344	0.2135 \pm 0.3788	0.2319 \pm 0.2488
PCR	2.0413\pm0.6646	0.4551\pm0.3845	0.5034\pm0.4221	1.4601\pm2.6607	0.1079\pm0.1087	0.2224\pm0.2472

Table 2: Ablation study (mean \pm std) on the ACIC benchmark. “*” marks the variants that PCR outperforms significantly at p-value < 0.01 over paired samples t-test.

		In-sample			Out-sample		
LPR	ISP	ϵ_{PEHE}	ϵ_{ATE}	ϵ_{ATT}	ϵ_{PEHE}	ϵ_{ATE}	ϵ_{ATT}
✗	✗	3.4288 \pm 0.3952*	1.1796 \pm 0.6443*	1.9186 \pm 0.8632*	3.3187 \pm 0.7622*	1.3581 \pm 1.0325*	1.4682 \pm 1.0636*
✓	✗	2.9668 \pm 0.9142	0.9162 \pm 0.5930	1.3961 \pm 0.9425	2.5193 \pm 0.7771	0.9164 \pm 0.8203	1.0020 \pm 0.8903
✗	✓	2.9341 \pm 0.7583	0.7825 \pm 0.5363	1.2473 \pm 0.7007	2.5983 \pm 0.7378*	0.8303 \pm 0.7695	0.9080 \pm 0.8328
✓	✓	2.6091\pm0.7673	0.5384\pm0.3932	1.0313\pm0.7206	2.0413\pm0.6640	0.4551\pm0.3845	0.5034\pm0.4221

4.2 Overall performance

Table 1 provides a comprehensive comparison of the PCR framework with various baseline methodologies. Key observations from this comparative analysis are outlined below:

- **Statistical Estimators:** This group exhibits strong performance on the PEHE metric. Neural network-based estimators particularly excel, surpassing linear models and random forests due to their enhanced ability to capture nonlinear relationships. Among them, TARNet, which integrates the strengths of both T-learner and S-learner, is noted for achieving the best overall performance within this group. However, its limitations in addressing treatment selection bias lead to its underperformance in certain scenarios.
- **Matching Methods:** Techniques such as PSM and O.Forest show robust capabilities in estimating average treatment effects, which contributes to their widespread adoption in policy evaluation contexts. However, their efficacy diminishes on the PEHE metric, restricting their suitability for applications requiring personalized treatment approaches, such as healthcare and advertising.
- **Representation-Based Methods:** These methods are particularly effective in mitigating treatment selection bias, thereby enhancing overall estimation accuracy. The SITE model, which emphasizes the preservation of local similarities, consistently outperforms the conventional TARNet approach. Furthermore, ESCFR, which achieves the best performance among the baselines with an out-of-sample PEHE of 2.678 on the ACIC dataset, utilizes an unbalanced Wasserstein discrepancy. However, its failure to handle the local proximity and the curse of dimensionality limits its effectiveness in fully overcoming treatment selection bias.
- **PCR:** PCR surpasses other prevalent baselines with significant improvements across most metrics. This superiority is attributed to the innovative LPR and ISP modules. These components enable PCR to adeptly handle both local proximity preservation and dimensionality challenges, which facilitates more accurate alignment of treatment groups and thereby handling of selection bias.

4.3 Ablation study

In Table 2, we examine the contributions of individual components of PCR on the ACIC benchmark. Our study builds upon the CFR-Wass model [49], a canonical approach that employs the Wasserstein

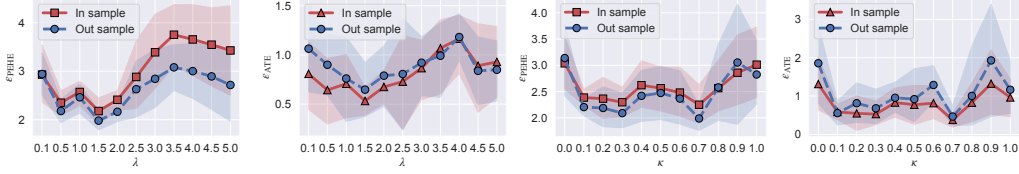


Figure 3: Parameter sensitivity of the LPR module on the ACIC dataset, with focus on λ (left and left center) and κ (right center and right). The lines and shaded areas indicate the mean values and 90% confidence intervals, respectively.

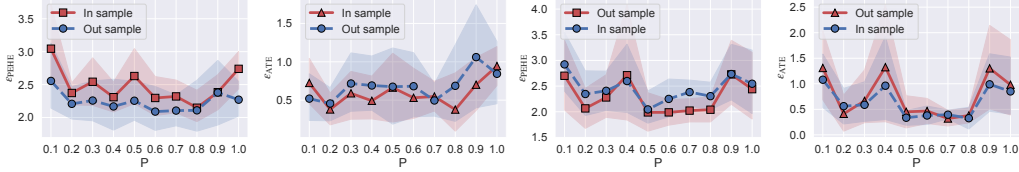


Figure 4: Parameter sensitivity of the ISP module on the ACIC dataset, where P stands for the ratio of dimensionality reduction. κ is set to 0.3 (left and left center) and 0.7 (right center and right). The lines and shaded areas indicate the mean values and 90% confidence intervals, respectively.

discrepancy to align treatment groups within the representation space. Firstly, we enhance CFR-Wass with LPR, which is particularly effective in reducing the out-of-sample PEHE to 2.5193, demonstrating the utility of maintaining local structures within learned representations. Next, we incorporate ISP designed to manage the curse of dimensionality when calculating discrepancies. Similarly, it enhances model performance, reducing the out-of-sample PEHE to 2.5983. Ultimately, PCR synthesizes both the LPR and ISP into a unified framework, as detailed in Section 3.3. It maintains the advantages of each individual component and achieves the best overall performance compared to other variants.

4.4 Analysis of the local proximity preservation regularizer

In this section, we analyze the efficacy of the proposed LPR component. There are two main hyperparameters in LPR: λ that controls the strength of distribution alignment and κ that controls the strength of LPR in (7). A sensitivity study for them is conducted in Figure 3, where the estimation error exhibits an reduction followed by an increase, with the increasing of both parameters. It reveals that both distribution alignment and LPR are effective to improve HTE estimation. However, overly emphasizing distribution balancing or local proximity preservation within a multi-task learning framework can result in compromised factual outcome estimation and, consequently, suboptimal treatment effect estimates.

4.5 Analysis of the informative subspace projector

In this section, we delve into the role of the ISP component. The characteristics of ISP are governed by the hyperparameter P, which dictates the extent of dimensionality reduction. We conduct a hyperparameter study for P in Figure 4, and the key observations are summarized below.

Dimensionality reduction effectively enhances model performance. Specifically, as P is decreased from 1 to 0.7, there is a notable improvement in the estimation accuracy, with the out-of-sample ϵ_{ATE} diminishing from approximately 0.8 to about 0.5. This improvement is primarily due to effective handling of the curse of dimensionality, which in turn facilitates a more accurate estimation of discrepancies using minibatch samples. However, excessive reduction in dimensionality can lead to substantial information loss, and thereby suboptimal estimates.

Interestingly, there is a relationship between the weighting parameter κ and the optimal setting for P. As κ increases, which shifts the discrepancy measure \mathbb{F} closer to the Gromov-Wasserstein discrepancy, the curse of dimensionality becomes more pronounced: the Gromov term relies heavily on unit-wise distances to compute local similarities, making dimensionality reduction increasingly

crucial. Consequently, the optimal P value tends to decrease with larger κ , underscoring the need to balance dimensionality reduction against the risk of significant information loss.

5 Related works

Current research in causal inference focuses on alleviating treatment selection bias by balancing distributions between treated and untreated groups. This can be achieved through three main methodological categories: reweighting-based, matching-based, and representation-based methods [32].

Reweighting-based methods primarily utilize propensity scores to achieve global balance between groups, involving the estimation of propensity scores and the construction of unbiased estimators [24, 32, 60]. Propensity scores are typically estimated using logistic regression [5, 12, 23, 70], with precision enhancements via feature selection [51, 58, 59], joint optimization [31, 70, 71], and alternative training techniques [75]. The inverse propensity score method exemplifies the unbiased estimator [45], although it suffers from high variance at low propensity scores and bias with incorrect estimates [25, 27, 56]. To mitigate these issues, doubly robust estimators and variance reduction techniques have been developed [16, 29, 44]. However, the reliance on propensity scores limits the practical application of these methods.

Matching-based methods construct locally balanced distributions by matching comparable units from different groups, based on various similarity measures. Propensity score matching, which uses estimated propensity scores for calculating unit (dis)similarity, is one such technique [46]. Tree-based methods, employing adaptive similarity measures, are also considered under this category [55]. Despite their effectiveness, the computational intensity of these methods restricts their scalability in large-scale applications [3, 35, 60].

Representation-based methods involve constructing a mapping to a feature space where distributional discrepancies are minimized, with initial approaches focusing on maximum mean discrepancy and vanilla Wasserstein discrepancy [19, 49]. Enhancements have been made by integrating local proximity preservation [67, 68], feature selection [6, 17], representation decomposition [17, 61], and adversarial training [69]. However, challenges such as outlier fluctuations [14] and unlabeled confounders [73] still undermine the reliability of these methods.

The recent advances of optimal transport (OT) in causality [52] has spawned innovative HTE estimators through sample reweighting [13, 64, 65] and matching [4]. A typically related line of works advocates building balanced representations with OT to which significantly enhances representation-based HTE estimators [33, 34, 57]. Li et al. [34] for instance use OT to align factual and counterfactual distributions; Wang et al. [57] apply OT to achieve HTE estimation while mitigating noise and unobserved confounding effects. Despite this progress, these approaches generally adhere to the traditional Kantorovich problem, similar to [49], focusing on global alignment while often neglecting both local proximity and the curse of dimensionality. Therefore, developing OT formulations to meet the unique property of HTE estimation remains a fruitful avenue for future research.

6 Conclusion

Representation learning has emerged as a pivotal approach for estimating individual treatment effects due to its efficacy in mitigating treatment selection bias. Despite the successes, current methods often overlook crucial aspects such as local proximity and the curse of dimensionality, which are essential for adequately addressing treatment selection bias. To bridge this gap, a principled approach known as PCR, based on a generalized OT problem, has been developed. Extensive experiments validate that PCR handles both problems effectively and outperforms prevalent baseline models.

Looking forward, two promising research avenues are identified. The first involves the integration of normalizing flows for representation mapping, prized for their invertibility, a property that is consistent with the foundational assumptions of counterfactual regression as posited by Shalit et al. [49]. The second avenue focuses on the practical application of our methodology to industrial contexts, specifically for bias mitigation in recommendation systems [56].

References

- [1] Artem Betlei, Eustache Diemert, and Massih-Reza Amini. Uplift modeling with generalization guarantees. In *SIGKDD*, pages 55–65, 2021.
- [2] Nicolas Bonneel, Michiel van de Panne, Sylvain Paris, and Wolfgang Heidrich. Displacement interpolation using lagrangian mass transport. *ACM Trans. Graph.*, 30(6):158, 2011.
- [3] Yale Chang and Jennifer G. Dy. Informative subspace learning for counterfactual inference. In *AAAI*, pages 1770–1776, 2017.
- [4] Arthur Charpentier, Emmanuel Flachaire, and Ewen Gallic. Optimal transport for counterfactual estimation: A method for causal inference. *arXiv preprint arXiv:2301.07755*, 2023.
- [5] Jiawei Chen, Hande Dong, Yang Qiu, Xiangnan He, Xin Xin, Liang Chen, Guli Lin, and Keping Yang. Autodebias: Learning to debias for recommendation. In *SIGIR*, pages 21–30, 2021.
- [6] Mingyuan Cheng, Xinru Liao, Quan Liu, Bin Ma, Jian Xu, and Bo Zheng. Learning disentangled representations for counterfactual regression via mutual information minimization. In *SIGIR*, pages 1802–1806, 2022.
- [7] Lénaïc Chizat, Pierre Roussillon, Flavien Léger, François-Xavier Vialard, and Gabriel Peyré. Faster wasserstein distance estimation with the sinkhorn divergence. In *NeurIPS*, 2020.
- [8] José M Cordero, Víctor Cristóbal, and Daniel Santfín. Causal inference on education policies: A survey of empirical studies using pisa, timss and pirls. *J. Econ. Surv.*, 32(3):878–915, 2018.
- [9] Nicolas Courty, Rémi Flamary, Devis Tuia, and Alain Rakotomamonjy. Optimal transport for domain adaptation. *IEEE Trans. Pattern Anal. Mach. Intell.*, 39(9):1853–1865, 2017.
- [10] Richard K Crump, V Joseph Hotz, Guido W Imbens, and Oscar A Mitnik. Nonparametric tests for treatment effect heterogeneity. *Rev. Econ. Stat.*, 90(3):389–405, 2008.
- [11] Marco Cuturi. Sinkhorn distances: Lightspeed computation of optimal transport. In *NeurIPS*, pages 2292–2300, 2013.
- [12] Quanyu Dai, Haoxuan Li, Peng Wu, Zhenhua Dong, Xiao-Hua Zhou, Rui Zhang, Rui Zhang, and Jie Sun. A generalized doubly robust learning framework for debiasing post-click conversion rate prediction. In *SIGKDD*, pages 252–262, 2022.
- [13] Eric Dunipace. Optimal transport weights for causal inference. *CoRR*, abs/2109.01991, 2021.
- [14] Kilian Fatras, Thibault Séjourné, Rémi Flamary, and Nicolas Courty. Unbalanced minibatch optimal transport; applications to domain adaptation. In *ICML*, volume 139, pages 3186–3197, 2021.
- [15] Damien François, Vincent Wertz, and Michel Verleysen. The concentration of fractional distances. *IEEE Trans. Knowl. Data Eng.*, 19(7):873–886, 2007.
- [16] Siyuan Guo, Lixin Zou, Yiding Liu, Wenwen Ye, Suqi Cheng, Shuaiqiang Wang, Hechang Chen, Dawei Yin, and Yi Chang. Enhanced doubly robust learning for debiasing post-click conversion rate estimation. In *SIGIR*, pages 275–284, 2021.
- [17] Negar Hassanpour and Russell Greiner. Learning disentangled representations for counterfactual regression. In *ICLR*. OpenReview.net, 2020.
- [18] Chen Huang, Chen Change Loy, and Xiaoou Tang. Local similarity-aware deep feature embedding. *Advances in neural information processing systems*, 29, 2016.
- [19] Fredrik D. Johansson, Uri Shalit, and David A. Sontag. Learning representations for counterfactual inference. In *ICML*, pages 3020–3029, 2016.
- [20] Leonid V Kantorovich. On the translocation of masses. *J. Math. Sci.*, 133(4):1381–1382, 2006.
- [21] Diederik P. Kingma and Jimmy Ba. Adam: A method for stochastic optimization. In *ICLR*, 2015.

- [22] Sören Reinhold Künzel, Jasjeet Sekhon, Peter Bickel, and Bin Yu. Metalearners for estimating heterogeneous treatment effects using machine learning. *Proc. Natl. Acad. Sci. U. S. A.*, 116(10):4156–4165, 2019.
- [23] Jae-woong Lee, Seongmin Park, and Jongwuk Lee. Dual unbiased recommender learning for implicit feedback. In *SIGIR*, pages 1647–1651, 2021.
- [24] Haoxuan Li, Chunyuan Zheng, Shuyi Wang, Kunhan Wu, Eric Wang, Peng Wu, Zhi Geng, Xu Chen, and Xiao-Hua Zhou. Relaxing the accurate imputation assumption in doubly robust learning for debiased collaborative filtering. In *ICML*.
- [25] Haoxuan Li, Quanyu Dai, Yuru Li, Yan Lyu, Zhenhua Dong, Peng Wu, and Xiao-Hua Zhou. Multiple robust learning for recommendation. *arXiv:2207.10796*, 2022.
- [26] Haoxuan Li, Yanghao Xiao, Chunyuan Zheng, and Peng Wu. Balancing unobserved confounding with a few unbiased ratings in debiased recommendations. In *WWW*, pages 305–315, 2022.
- [27] Haoxuan Li, Yanghao Xiao, Chunyuan Zheng, Peng Wu, and Peng Cui. Propensity matters: Measuring and enhancing balancing for recommendation. In *ICML*, volume 202 of *Proceedings of Machine Learning Research*, pages 20182–20194. PMLR, 2023.
- [28] Haoxuan Li, Chunyuan Zheng, Yixiao Cao, Zhi Geng, Yue Liu, and Peng Wu. Trustworthy policy learning under the counterfactual no-harm criterion. In *ICML*, volume 202 of *Proceedings of Machine Learning Research*, pages 20575–20598. PMLR, 2023.
- [29] Haoxuan Li, Chunyuan Zheng, and Peng Wu. Stabledr: Stabilized doubly robust learning for recommendation on data missing not at random. In *ICLR*, 2023.
- [30] Haoxuan Li, Chunyuan Zheng, Peng Wu, Kun Kuang, Yue Liu, and Peng Cui. Who should be given incentives? counterfactual optimal treatment regimes learning for recommendation. In *KDD*, pages 1235–1247. ACM, 2023.
- [31] Haoxuan Li, Kunhan Wu, Chunyuan Zheng, Yanghao Xiao, Hao Wang, Zhi Geng, Fuli Feng, Xiangnan He, and Peng Wu. Removing hidden confounding in recommendation: a unified multi-task learning approach. *NeurIPS*, 36, 2024.
- [32] Haoxuan Li, Chunyuan Zheng, Wenjie Wang, Hao Wang, Fuli Feng, and Xiao-Hua Zhou. Debiased recommendation with noisy feedback. In *SIGKDD*, 2024.
- [33] Qian Li, Zhichao Wang, Shaowu Liu, Gang Li, and Guandong Xu. Deep treatment-adaptive network for causal inference. *VLDBJ*, pages 1–16, 2022.
- [34] Qian Li, Zhichao Wang, Shaowu Liu, Gang Li, and Guandong Xu. Causal optimal transport for treatment effect estimation. *IEEE Trans. Neural Networks Learn. Syst.*, 34(8):4083–4095, 2023.
- [35] Sheng Li, Nikos Vlassis, Jaya Kawale, and Yun Fu. Matching via dimensionality reduction for estimation of treatment effects in digital marketing campaigns. In *IJCAI*, pages 3768–3774, 2016.
- [36] Tianyi Lin, Chenyou Fan, Nhat Ho, Marco Cuturi, and Michael Jordan. Projection robust wasserstein distance and riemannian optimization. *Advances in neural information processing systems*, 33:9383–9397, 2020.
- [37] Facundo Mémoli. Gromov–wasserstein distances and the metric approach to object matching. *Foundations of computational mathematics*, 11:417–487, 2011.
- [38] Gaspard Monge. Mémoire sur la théorie des déblais et des remblais. *Mem. Math. Phys. Acad. Royale Sci.*, pages 666–704, 1781.
- [39] X Nie and S Wager. Quasi-oracle estimation of heterogeneous treatment effects. *Biometrika*, 108(2):299–319, 2020.

- [40] Kenneth R Niswander and Myron Gordon. *The women and their pregnancies: the Collaborative Perinatal Study of the National Institute of Neurological Diseases and Stroke*, volume 73. National Institute of Health, 1972.
- [41] Judea Pearl and Dana Mackenzie. *The book of why: the new science of cause and effect*. Basic books, 2018.
- [42] Ofir Pele and Michael Werman. Fast and robust earth mover’s distances. In *ICCV*, pages 460–467, 2009.
- [43] Gabriel Peyré and Marco Cuturi. Computational optimal transport. *Found. Trends Mach. Learn.*, 11(5-6):355–607, 2019.
- [44] James M Robins, Andrea Rotnitzky, and Lue Ping Zhao. Estimation of regression coefficients when some regressors are not always observed. *J. Am. Stat. Assoc.*, 89(427):846–866, 1994.
- [45] Paul Rosenbaum and Donald B Rubin. The central role of the propensity score in observational studies for causal effects. *Biometrika*, 70(1):41–55, 1983.
- [46] Paul Rosenbaum and Donald B Rubin. The central role of the propensity score in observational studies for causal effects. *Biometrika*, 70(1):41–55, 1983.
- [47] Donald B Rubin. Estimating causal effects of treatments in randomized and nonrandomized studies. *J. Educ. Psychol.*, 66(5):688, 1974.
- [48] Patrick Schwab, Lorenz Linhardt, Stefan Bauer, Joachim Buhmann, and Walter Karlen. Learning counterfactual representations for estimating individual dose-response curves. In *AAAI*, pages 5612–5619, 2020.
- [49] Uri Shalit, Fredrik D. Johansson, and David Sontag. Estimating individual treatment effect: generalization bounds and algorithms. In *ICML*, pages 3076–3085, 2017.
- [50] Claudia Shi, David M. Blei, and Victor Veitch. Adapting neural networks for the estimation of treatment effects. In *NeurIPS*, pages 2503–2513, 2019.
- [51] Susan M Shortreed and Ashkan Ertefaie. Outcome-adaptive lasso: variable selection for causal inference. *Biometrics*, 73(4):1111–1122, 2017.
- [52] Ruibo Tu, Kun Zhang, Hedvig Kjellström, and Cheng Zhang. Optimal transport for causal discovery. In *ICLR*. OpenReview.net, 2022.
- [53] Titouan Vayer, Laetitia Chapel, Rémi Flamary, Romain Tavenard, and Nicolas Courty. Fused gromov-wasserstein distance for structured objects. *Algorithms*, 13(9):212, 2020.
- [54] Cédric Villani. *Optimal transport: old and new*, volume 338. Springer, 2009.
- [55] Stefan Wager and Susan Athey. Estimation and inference of heterogeneous treatment effects using random forests. *J. Am. Stat. Assoc.*, 113(523):1228–1242, 2018.
- [56] Hao Wang, Tai-Wei Chang, Tianqiao Liu, Jianmin Huang, Zhichao Chen, Chao Yu, Ruopeng Li, and Wei Chu. Escm^2 : Entire space counterfactual multi-task model for post-click conversion rate estimation. In *SIGIR*, 2022.
- [57] Hao Wang, Jiajun Fan, Zhichao Chen, Haoxuan Li, Weiming Liu, Tianqiao Liu, Quanyu Dai, Yichao Wang, Zhenhua Dong, and Ruiming Tang. Optimal transport for treatment effect estimation. *Advances in Neural Information Processing Systems*, 36, 2024.
- [58] Haotian Wang, Kun Kuang, Haoang Chi, Longqi Yang, Mingyang Geng, Wanrong Huang, and Wenjing Yang. Treatment effect estimation with adjustment feature selection. In *KDD*, pages 2290–2301. ACM, 2023.
- [59] Haotian Wang, Kun Kuang, Long Lan, Zige Wang, Wanrong Huang, Fei Wu, and Wenjing Yang. Out-of-distribution generalization with causal feature separation. *IEEE Trans. Knowl. Data Eng.*, 2023.

- [60] Anpeng Wu, Kun Kuang, Ruoxuan Xiong, Bo Li, and Fei Wu. Stable estimation of heterogeneous treatment effects. In *ICML*, volume 202 of *Proceedings of Machine Learning Research*, pages 37496–37510. PMLR, 2023.
- [61] Anpeng Wu, Junkun Yuan, Kun Kuang, Bo Li, Runze Wu, Qiang Zhu, Yueting Zhuang, and Fei Wu. Learning decomposed representations for treatment effect estimation. *IEEE Trans. Knowl. Data Eng.*, 35(5):4989–5001, 2023.
- [62] Peng Wu, Haoxuan Li, Yuhao Deng, Wenjie Hu, Quanyu Dai, Zhenhua Dong, Jie Sun, Rui Zhang, and Xiao-Hua Zhou. On the opportunity of causal learning in recommendation systems: Foundation, estimation, prediction and challenges. In *IJCAI*, pages 23–29, 2022.
- [63] Hongteng Xu, Dixin Luo, and Lawrence Carin. Scalable gromov-wasserstein learning for graph partitioning and matching. *Advances in neural information processing systems*, 32, 2019.
- [64] Yuguang Yan, Zeqin Yang, Weilin Chen, Ruichu Cai, Zhifeng Hao, and Michael Kwok-Po Ng. Exploiting geometry for treatment effect estimation via optimal transport. In *AAAI*, volume 38, pages 16290–16298, 2024.
- [65] Hao Yang, Zexu Sun, Hongteng Xu, and Xu Chen. Revisiting counterfactual regression through the lens of gromov-wasserstein information bottleneck. *arXiv preprint arXiv:2405.15505*, 2024.
- [66] Mengyue Yang, Xinyu Cai, Furui Liu, Weinan Zhang, and Jun Wang. Specify robust causal representation from mixed observations. In *KDD*, pages 2978–2987. ACM, 2023.
- [67] Liuyi Yao, Sheng Li, Yaliang Li, Mengdi Huai, Jing Gao, and Aidong Zhang. Representation learning for treatment effect estimation from observational data. In *NeurIPS*, pages 2638–2648, 2018.
- [68] Liuyi Yao, Sheng Li, Yaliang Li, Mengdi Huai, Jing Gao, and Aidong Zhang. ACE: adaptively similarity-preserved representation learning for individual treatment effect estimation. In *ICDM*, pages 1432–1437, 2019.
- [69] Jinsung Yoon, James Jordon, and Mihaela van der Schaar. GANITE: estimation of individualized treatment effects using generative adversarial nets. In *ICLR*, 2018.
- [70] Wenhao Zhang, Wentian Bao, Xiao-Yang Liu, Keping Yang, Quan Lin, Hong Wen, and Ramin Ramezani. Large-scale causal approaches to debiasing post-click conversion rate estimation with multi-task learning. In *WWW*, pages 2775–2781, 2020.
- [71] Yang Zhang, Dong Wang, Qiang Li, Yue Shen, Ziqi Liu, Xiaodong Zeng, Zhiqiang Zhang, Jinjie Gu, and Derek F Wong. User retention: A causal approach with triple task modeling. In *IJCAI*, 2021.
- [72] Zhengxin Zhang, Ziv Goldfeld, Youssef Mroueh, and Bharath K Sriperumbudur. Gromov-wasserstein distances: Entropic regularization, duality, and sample complexity. *arXiv preprint arXiv:2212.12848*, 2022.
- [73] Jiajing Zheng. *Sensitivity Analysis for Causal Inference with Unobserved Confounding*. University of California, Santa Barbara, 2021.
- [74] Kailiang Zhong, Fengtong Xiao, Yan Ren, Yaorong Liang, Wenqing Yao, Xiaofeng Yang, and Ling Cen. Descn: Deep entire space cross networks for individual treatment effect estimation. In *Proceedings of the 28th ACM SIGKDD Conference on Knowledge Discovery and Data Mining*, pages 4612–4620, 2022.
- [75] Ziwei Zhu, Yun He, Yin Zhang, and James Caverlee. Unbiased implicit recommendation and propensity estimation via combinatorial joint learning. In *RecSys*, pages 551–556, 2020.

A Heterogeneous treatment effect estimation with observational data

In this section, we introduce essential preliminaries concerning HTE estimation, aimed at readers new to this field. We subsequently elucidate our theoretical contributions based on these foundational concepts.

A.1 Problem formulation

Here, we formalize the definitions, assumptions, and pertinent lemmas in the domain of HTE estimation from observational data. Building on the notations introduced in Section 2.1, consider an individual with covariates x exhibiting two potential outcomes: $Y_1(x)$ if treated and $Y_0(x)$ otherwise. The core of causal inference, the individual treatment effect (CATE), is defined as the difference between these outcomes.

Definition A.1. *The individual treatment effect (CATE) for a unit with covariates x is defined as:*

$$\tau(x) := \mathbb{E}[Y_1 - Y_0 \mid x], \quad (11)$$

where $Y_1(x)$ and $Y_0(x)$ are abbreviated to Y_1 and Y_0 , respectively, for brevity, and the expectation is computed over the potential outcome space \mathcal{Y} .

Estimating CATE using observational data presents notable challenges:

- **Missing counterfactuals:** Only the factual outcome is observable; e.g., if a patient is treated, the outcome had they not been treated remains unknown.
- **Treatment selection bias:** Individuals might not be randomly assigned to treatments, leading to non-comparability between treated and untreated groups. For instance, doctors may choose different treatments based on a patient’s health status, making the two groups inherently heterogeneous.

Pearl and Mackenzie [41] propose a two-step methodology to address these issues: identification and estimation. The identification step involves constructing an unbiased statistical estimand to identify the causal estimand (e.g., $\tau(x)$), contingent on certain assumptions being met.

Assumption A.1. *(Unconfoundedness) For all covariates x in the population of interest, potential outcomes (Y_0, Y_1) are conditionally independent of the treatment assignment given $X = x$.*

Assumption A.2. *(Consistency) The observed outcome Y is consistent with the potential outcome corresponding to the assigned treatment, across all covariates x .*

Assumption A.3. *(Positivity) Each individual has a nonzero probability of receiving each treatment, formally, $0 < \rho(T = 1 \mid X = x) < 1$ for all x .*

Assumption A.4. *(SUTVA) The potential outcomes for any individual are unaffected by the treatment assignments of others, and there are no varying versions of the treatment that could result in different outcomes.*

The estimation step seeks to estimate the unbiased estimand using observational data. Lemma A.1 demonstrates how these assumptions facilitate CATE estimation.

Lemma A.1. *The CATE $\tau(x)$ can be identified by:*

$$\begin{aligned} \mathbb{E}[Y_1 - Y_0 \mid X = x] &= \mathbb{E}[Y_1 \mid X = x, T = 1] - \mathbb{E}[Y_0 \mid X = x, T = 0] \\ &= \mathbb{E}[Y \mid X = x, T = 1] - \mathbb{E}[Y \mid X = x, T = 0], \end{aligned} \quad (12)$$

leveraging the unconfoundedness and consistency assumptions. This statistical framework depends critically on the positivity assumption; violating it renders certain estimations infeasible, as detailed in the ensuing equations.

A.2 Meta-learners for CATE estimation with observational data

To address the issue of missing counterfactuals, existing meta-learner based methods decompose the challenge of CATE estimation into manageable subproblems, each solvable using standard supervised learning techniques [22, 39]. These methods capitalize on the structure of the data and the implicit relationships between treatment effects and covariates.

Definition A.2. Let $\psi : \mathcal{S}_X \rightarrow \mathcal{S}_R$ denote a representation mapping that transforms covariates X into a representation space $R = \psi(X)$. Define $\phi_T : \mathcal{R} \times \mathcal{T} \rightarrow \mathcal{Y}$ as an outcome mapping that correlates these representations and treatment states to their respective factual outcomes, with $Y_1 = \phi_1(R)$ and $Y_0 = \phi_0(R)$.

Assumption A.5. The mapping $\phi : \mathcal{S}_X \rightarrow \mathcal{S}_R$ is both differentiable and invertible, with the inverse ϕ^{-1} defined over the representation space \mathcal{S}_R .

Meta-learner methodologies such as the S-learner and T-learner provide foundational strategies:

- **S-learner** integrates the treatment indicator T directly into the covariate set X , utilizing a unified representation mapping ψ and outcome mapping ϕ to estimate outcomes. This approach might underperform when treatment effects are subtle due to its inability to emphasize the treatment indicator within its network structure.
- **T-learner** constructs separate models for treated (X_1) and untreated (X_0) units, thus emphasizing the treatment effect but at the cost of reduced data efficiency, which may limit its application in scenarios with small datasets.

The TARNet model [49] synergizes the strengths of both the T-learner and S-learner by utilizing a shared representation mapping ψ and distinct outcome mappings ϕ_1 and ϕ_0 for treated and untreated units, respectively. It estimates the CATE as follows:

$$\hat{\tau}_{\psi, \phi}(X) := \hat{Y}_1 - \hat{Y}_0, \quad \text{where } \hat{Y}_1 = \phi_1(\psi(X)), \quad \hat{Y}_0 = \phi_0(\psi(X)), \quad (13)$$

optimizing the factual error $\epsilon_F(\phi, \psi)$ defined in Definition A.4.

Definition A.3. Let \mathbb{L} represent the loss function, e.g., squared loss, measuring the quality of outcome predictions, we have:

$$l_{\psi, \phi}(x, t) := \int \mathbb{L}(Y_t, \phi(\psi(x), t)) \cdot \rho(Y_t | x) dY_t, \quad (14)$$

where $\mathbb{L}(Y_t, \phi(\psi(x), t)) = (Y_t - \phi(\psi(x), t))^2$.

The performance of this CATE estimator is primarily assessed using the Precision in Estimation of Heterogeneous Effects (PEHE):

$$\epsilon_{\text{PEHE}}(\psi, \phi) := \int (\hat{\tau}_{\psi, \phi}(x) - \tau(x))^2 \rho(x) dx, \quad (15)$$

highlighting the effectiveness of TARNet in providing a nuanced approach to estimating CATE that bridges the benefits of both foundational meta-learner models.

Definition A.4. Let \mathbb{L} be the loss function that measures the quality of outcome estimation, e.g., the squared loss. The expected loss for the units with covariates x and treatment indicator t is:

$$l_{\psi, \phi}(x, t) := \int \mathbb{L}(Y_t, \phi(\psi(x), t)) \cdot \rho(Y_t | x) dY_t. \quad (16)$$

where \mathbb{L} is realized with the squared loss: $\mathbb{L}(Y_t, \psi(\phi(x), t)) = (Y_t - \psi(\phi(x), t))^2$ in our scenario. The expected factual outcome estimation error for treated, untreated and all units are:

$$\begin{aligned} \epsilon_F^{\text{T}=1}(\psi, \phi) &:= \int l_{\psi, \phi}(x, 1) \cdot \rho^{\text{T}=1}(x) dx, \\ \epsilon_F^{\text{T}=0}(\psi, \phi) &:= \int l_{\psi, \phi}(x, 0) \cdot \rho^{\text{T}=0}(x) dx, \\ \epsilon_F(\psi, \phi) &:= \int l_{\psi, \phi}(x, t) \cdot \rho(x, t) dx dt. \end{aligned} \quad (17)$$

A.3 Representation-based methods for treatment selection bias

Treatment selection bias presents significant challenges in causal inference by causing covariate distributions to differ markedly between treated and untreated groups. This discrepancy can lead to models that overfit to characteristics specific to one group and fail to generalize across the population. For instance, a potential outcome estimator ϕ_1 trained exclusively on treated units may perform poorly when applied to untreated units, leading to biased estimates of $\hat{\tau}$, as illustrated in Figure 1(a).

Definition A.5. Let $\rho^{T=1}(x)$ and $\rho^{T=0}(x)$ denote the covariate distributions for the treated and untreated groups, respectively. Define $\rho_\psi^{T=1}(r)$ and $\rho_\psi^{T=0}(r)$ as the distributions of the representations $r = \psi(x)$, where ψ is the representation mapping detailed in Definition 2.2.

To address treatment selection bias, representation-based approaches, such as those proposed by Johansson et al. [19], Shalit et al. [49], aim to minimize the distribution discrepancies in the representation space. These methods often employ the Integral Probability Metric (IPM) to measure distribution differences effectively.

Definition A.6. Given two distribution functions $\rho^{T=1}(x)$ and $\rho^{T=0}(x)$ supported over \mathcal{X} , and a sufficiently large function family \mathcal{F} , the Integral Probability Metric (IPM) induced by \mathcal{F} is defined as:

$$\text{IPM}_{\mathcal{F}}(\rho^{T=1}, \rho^{T=0}) = \sup_{f \in \mathcal{F}} \left| \int f(x) (\rho^{T=1}(x) - \rho^{T=0}(x)) dx \right|, \quad (18)$$

These methods not only focus on reducing the factual outcome estimation error ϵ_F but also on minimizing the IPM between the learned representations of treated and untreated groups, thereby aligning the covariate distributions in the latent space to enhance the generalizability of the treatment effect estimates.

Theorem A.1. Assuming mappings ψ and ϕ as defined in Definition 2.2, and \mathcal{F} a predefined function family sufficiently large to include $\frac{1}{B_\psi} \cdot l_{\psi, \phi}(x, t)$ for $t \in \{0, 1\}$, Shalit et al. [49] demonstrate that:

$$\epsilon_{\text{PEHE}}(\psi, \phi) \leq 2 \left(\epsilon_F^{T=0}(\psi, \phi) + \epsilon_F^{T=1}(\psi, \phi) + B_\psi \text{IPM}_{\mathcal{F}}(\rho_\psi^{T=1}, \rho_\psi^{T=0}) - 2\sigma_Y^2 \right), \quad (19)$$

where $\epsilon_F^{T=0}$ and $\epsilon_F^{T=1}$ are defined according to Definition A.4, and $\rho_\psi^{T=1}(r)$ and $\rho_\psi^{T=0}(x)$ are specified in Definition A.5.

This theorem underpins the effectiveness of using representation-based methods to mitigate bias induced by treatment selection, thereby improving the reliability and accuracy of estimated treatment effects.

A.4 Theoretical results

While Theorem A.1 provides a foundational framework for addressing biases in treatment effect estimation using representation-based methods, two significant challenges require further exploration.

Tractability of the IPM Metric: Despite the profound theoretical properties of the Integral Probability Metric (IPM), its direct computation can be intractable for complex distributions. However, within certain function families \mathcal{F} , such as the family of 1-Lipschitz functions, the IPM can be equivalently expressed as the Wasserstein distance through the Kantorovich-Rubinstein duality, a concept extensively documented in the literature [49, 54]. This equivalence allows for practical computation of the IPM as the Wasserstein discrepancy, detailed in the following lemma:

Lemma A.2. Given two distribution functions $\rho_1(x)$ and $\rho_2(x)$ supported over \mathcal{X} , and letting \mathcal{F} be the family of 1-Lipschitz functions, the IPM induced by \mathcal{F} is equivalent to the Wasserstein distance \mathbb{W} , as demonstrated by Villani [54]:

$$\text{IPM}_{\mathcal{F}}(\rho_1, \rho_2) = \mathbb{W}(\rho_1, \rho_2). \quad (20)$$

Sampling Complexity of Discrepancy Measures: Theorem A.1 assumes access to the entire populations of treated and untreated groups to calculate the distribution discrepancy. However, in practical machine learning scenarios, especially in deep learning, parameters are often updated using stochastic gradient methods on mini-batches of data rather than the full dataset. This raises questions about the validity of Theorem A.1 when applied at the mini-batch level.

Recent studies have explored the sample complexity of various discrepancy measures such as the Wasserstein distance and Gromov discrepancy, providing insights into their behavior with limited sample sizes [7, 72], as encapsulated in Lemma A.3 and A.4. Building on these insights, we innovatively propose Theorem A.2, which extends Theorem A.1 to a specific Fused Gromov-Wasserstein (FGW) discrepancy employed in this work, examining its sample complexity when only a small minibatch sample is available.

Lemma A.3. Consider two measures α and β with compact supports $\mathcal{S}_\alpha \in \mathbb{R}^d$ and $\mathcal{S}_\beta \in \mathbb{R}^d$. Let $C = \text{diam}(\mathcal{S}_\alpha) \vee \text{diam}(\mathcal{S}_\beta)$, considering the case where $d > 4$, we have:

$$\mathbb{E} \left[\left| \mathbb{W}(\alpha, \beta)^2 - \mathbb{W}(\hat{\alpha}_n, \hat{\beta}_n)^2 \right| \right] \lesssim n^{-\frac{2}{d}}, \quad (21)$$

where the notation \lesssim hides constants that is independent to the number of samples n . α_n and β_n are empirical distributions of α and β with n i.i.d. samples.

Lemma A.4. Consider two measures α and β with compact supports $\mathcal{S}_\alpha \in \mathbb{R}^d$ and $\mathcal{S}_\beta \in \mathbb{R}^d$. Let $C = \text{diam}(\mathcal{S}_\alpha) \vee \text{diam}(\mathcal{S}_\beta)$, considering the case where $d > 4$, we have:

$$\mathbb{E} \left[\left| \mathbb{G}(\alpha, \beta)^2 - \mathbb{G}(\hat{\alpha}_n, \hat{\beta}_n)^2 \right| \right] \lesssim \frac{C^4}{\sqrt{n}} + (1 + C^4) n^{-\frac{2}{d}}, \quad (22)$$

where the notation \lesssim hides constants that is independent to the number of samples n . α_n and β_n are empirical distributions of α and β with n i.i.d. samples.

Theorem A.2. Let ψ and ϕ be the representation mapping and factual outcome mapping, respectively; $\hat{\mathbb{W}}_\psi$ be the group discrepancy at a mini-batch level. With the probability of at least $1 - \delta$, we have:

$$\epsilon_{\text{PEHE}}(\psi, \phi) \leq 2 \left[\epsilon_{\mathbb{F}}^{T=1}(\psi, \phi) + \epsilon_{\mathbb{F}}^{T=0}(\psi, \phi) + B_{\psi, \kappa} \mathbb{F}(\mathcal{R}_\psi^{T=0}, \mathcal{R}_\psi^{T=1}) - 2\sigma_Y^2 + \mathcal{O}(N^{-\frac{2}{d}}) \right], \quad (23)$$

where $\epsilon_{\mathbb{F}}^{T=1}$ and $\epsilon_{\mathbb{F}}^{T=0}$ are the expected errors of factual outcome estimation, N is the batch size, σ_Y^2 is the variance of outcomes, $B_{\psi, \kappa}$ is a constant term, and $\mathcal{O}(\cdot)$ is a sampling complexity term.

Proof. According to Theorem A.1 we have:

$$\epsilon_{\text{PEHE}}(\psi, \phi) \leq 2 \left(\epsilon_{\mathbb{F}}^{T=0}(\psi, \phi) + \epsilon_{\mathbb{F}}^{T=1}(\psi, \phi) + B_\psi \text{IPM}_{\mathcal{F}}(\rho_\psi^{T=1}, \rho_\psi^{T=0}) - 2\sigma_Y^2 \right). \quad (24)$$

Assuming that there exists a constant $B_\psi > 0$, such that for $t \in \{0, 1\}$, $\frac{1}{B_\psi} \cdot l_{\psi, \phi}(x, t)$ belongs to the family of 1-Lipschitz functions. According to Lemma A.2, we have

$$\epsilon_{\text{PEHE}}(\psi, \phi) \leq 2 \left(\epsilon_{\mathbb{F}}^{T=0}(\psi, \phi) + \epsilon_{\mathbb{F}}^{T=1}(\psi, \phi) + B_\psi \mathbb{W}(\rho_\psi^{T=1}, \rho_\psi^{T=0}) - 2\sigma_Y^2 \right). \quad (25)$$

Following Definition 2.3, let $\mathcal{R}_\psi^{T=1}$ and $\mathcal{R}_\psi^{T=0}$ be the empirical distributions of representations at a mini-batch level, both containing n units. Then, according to Lemma A.3 and A.4, we have:

$$\begin{aligned} \mathbb{W}(\rho_\psi^{T=1}, \rho_\psi^{T=0}) &\leq \frac{1}{\kappa} \left(\kappa * \mathbb{W}(\rho_\psi^{T=1}, \rho_\psi^{T=0}) + (1 - \kappa) * \mathbb{G}(\rho_\psi^{T=1}, \rho_\psi^{T=0}) \right) \\ &\leq \frac{1}{\kappa} \left(\kappa * \mathbb{W}(\mathcal{R}_\psi^{T=1}, \mathcal{R}_\psi^{T=0}) + (1 - \kappa) * \mathbb{G}(\mathcal{R}_\psi^{T=1}, \mathcal{R}_\psi^{T=0}) + \frac{C^4}{\sqrt{n}} + (2 + C^4) n^{-\frac{2}{d}} \right) \\ &\leq \frac{1}{\kappa} \left(\mathbb{F}(\mathcal{R}_\psi^{T=1}, \mathcal{R}_\psi^{T=0}) + \frac{C^4}{\sqrt{n}} + (2 + C^4) n^{-\frac{2}{d}} \right), \end{aligned} \quad (26)$$

where \mathbb{W} denotes the Wasserstein discrepancy, \mathbb{G} denotes the Gromov discrepancy, \mathbb{F} denotes the fused Wasserstein discrepancy. These discrepancies will be introduced in the next section. Notably, there are two terms in the cost function of \mathbb{F} as per (37), which corresponding to the cost functions of \mathbb{W} and \mathbb{G} , respectively. Therefore, \mathbb{W} and \mathbb{G} can be viewed as minimizing the two terms of the cost function of \mathbb{F} individually, which often yields smaller values.

Denote $B_{\psi, \kappa} = B_\psi / \kappa$. Combing (26) and (25), we have

$$\epsilon_{\text{PEHE}}(\psi, \phi) \leq 2 \left[\epsilon_{\mathbb{F}}^{T=1}(\psi, \phi) + \epsilon_{\mathbb{F}}^{T=0}(\psi, \phi) + B_{\psi, \kappa} \mathbb{F}(\mathcal{R}_\psi^{T=0}, \mathcal{R}_\psi^{T=1}) - 2\sigma_Y^2 + \mathcal{O}(n^{-\frac{2}{d}}) \right], \quad (27)$$

where $\mathcal{O}(n^{-\frac{2}{d}}) = \frac{1}{\kappa} \left(\frac{C^4}{\sqrt{n}} + (2 + C^4) n^{-\frac{2}{d}} \right)$. The proof is completed. \square

B Discrete Optimal Transport

This section introduces the foundational concepts and algorithms necessary for computing optimal transport between discrete measures. We focus solely on discrete measures, as the general measures case extends beyond the scope of this paper [38]. For further exploration of this area, the reader is referred to seminal works in the literature [11, 43].

Algorithm 1 Sinkhorn Algorithm

Input: discrete measures $\alpha = \sum_{i=1}^n \mathbf{a}_i \delta_{\mathbf{x}_i}$ and $\beta = \sum_{j=1}^m \mathbf{b}_j \delta_{\mathbf{x}_j}$, distance matrix $\mathbf{D}_{ij} = \|\mathbf{x}_i - \mathbf{x}_j\|_2^2$.

Parameter: ϵ : strength of entropic regularization; ℓ_{\max} : maximum iterations.

Output: π^ϵ : the entropic regularized optimal transport matrix.

- 1: $\mathbf{K} \leftarrow \exp(-\mathbf{D}/\epsilon)$
 - 2: $\mathbf{u} \leftarrow \mathbf{1}_n, \mathbf{v} \leftarrow \mathbf{1}_m, \ell \leftarrow 1$
 - 3: **while** $\ell < \ell_{\max}$ **do**
 - 4: $\mathbf{u} \leftarrow \mathbf{a}/(\mathbf{K}\mathbf{v})$
 - 5: $\mathbf{v} \leftarrow \mathbf{b}/(\mathbf{K}^\top \mathbf{u})$
 - 6: $\ell \leftarrow \ell + 1$
 - 7: $\pi^\epsilon \leftarrow \text{diag}(\mathbf{u})\mathbf{K} \text{diag}(\mathbf{v})$
-

B.1 Notations and problem formulation

We consider a scenario involving n warehouses and m factories, where the i -th warehouse holds \mathbf{a}_i units of material and the j -th factory requires \mathbf{b}_j units of material [43]. The objective is to establish a mapping from warehouses to factories that: (1) completely allocates all warehouse materials, (2) fulfills all factory demands, and (3) restricts the transportation from each warehouse to at most one factory. Each potential mapping is evaluated based on a global cost, which aggregates the local costs incurred from transporting a unit of material from warehouse i to factory j .

Definition B.1. *The Monge problem for discrete measures, where $\alpha = \sum_{i=1}^n \mathbf{a}_i \delta_{\mathbf{x}_i}$ and $\beta = \sum_{j=1}^m \mathbf{b}_j \delta_{\mathbf{x}_j}$, seeks a mapping $\mathbb{T} : \{\mathbf{x}_i\}_{i=1}^n \rightarrow \{\mathbf{x}_j\}_{j=1}^m$ that optimally redistributes the mass from α to β . Specifically, for each j , it must hold that $\mathbf{b}_j = \sum_{i:\mathbb{T}(\mathbf{x}_i)=\mathbf{x}_j} \mathbf{a}_i$ and $\mathbb{T}_\# \alpha = \beta$. The goal is to minimize the transportation cost, represented by $c(x, y)$, leading to the following formulation:*

$$\min_{\mathbb{T}:\mathbb{T}_\# \alpha = \beta} \left\{ \sum_i c(\mathbf{x}_i, \mathbb{T}(\mathbf{x}_i)) \right\}. \quad (28)$$

This problem setup also facilitates the comparison of two probability measures where $\sum_i \mathbf{a}_i = \sum_j \mathbf{b}_j = 1$. The original Monge formulation does not guarantee the existence or uniqueness of solutions [43]. Therefore, Kantorovich [20] extended this framework by relaxing the one-to-one mapping constraint, allowing transportation from a single warehouse to multiple factories, and reformulated the problem as a linear programming challenge.

Definition B.2. *The Kantorovich problem for discrete measures α and β defines a cost-minimization task over feasible transport plans $\pi \in \mathbb{R}_+^{n \times m}$. The objective is to find a plan that minimizes the overall transport cost:*

$$\mathbb{W}(\alpha, \beta) := \min_{\pi \in \Pi(\alpha, \beta)} \langle \mathbf{D}, \pi \rangle, \quad \Pi(\alpha, \beta) := \left\{ \pi \in \mathbb{R}_+^{n \times m} : \pi \mathbf{1}_m = \mathbf{a}, \pi^\top \mathbf{1}_n = \mathbf{b} \right\}, \quad (29)$$

where $\mathbb{W}(\alpha, \beta)$ represents the Wasserstein discrepancy between α and β ; \mathbf{D} denotes the distance matrix computed using the squared Euclidean metric [9], and \mathbf{a}, \mathbf{b} are vectors describing the mass distribution in α and β , respectively.

B.2 Entropy-regularized optimal transport and Sinkhorn algorithm

Computing exact solutions to the Kantorovich problem is computationally intensive, typically involving methods like the interior-point or network-simplex which exhibit a complexity of $\mathcal{O}(n^3 \log n)$ [42]. A more efficient approach incorporates an entropic regularizer into the optimization, reducing computational complexity significantly. This regularization transforms the optimization problem into an ϵ -convex problem, which is amenable to solution by the Sinkhorn algorithm [11], reducing the complexity to $\mathcal{O}(n^2/\epsilon^2)$. This approach is not only computationally advantageous but also conducive to acceleration using GPUs due to its reliance on matrix-vector operations.

$$\mathbb{W}^\epsilon(\alpha, \beta) := \langle \mathbf{D}, \pi^\epsilon \rangle, \quad \pi^\epsilon := \arg \min_{\pi \in \Pi(\alpha, \beta)} \langle \mathbf{D}, \pi \rangle - \epsilon \mathbb{H}(\pi), \quad \mathbb{H}(\pi) := - \sum_{i,j} \pi_{ij} (\log(\pi_{ij}) - 1), \quad (30)$$

The Lagrangian for this regularized problem, defined in terms of Lagrange multipliers $\mathbf{f} \in \mathbb{R}^n$ and $\mathbf{g} \in \mathbb{R}^m$, is given by:

$$\Phi(\boldsymbol{\pi}, \mathbf{f}, \mathbf{g}) = \langle \mathbf{D}, \boldsymbol{\pi} \rangle - \epsilon \text{H}(\boldsymbol{\pi}) - \langle \mathbf{f}, \boldsymbol{\pi} \mathbf{1}_n - \mathbf{a} \rangle - \langle \mathbf{g}, \boldsymbol{\pi}^\top \mathbf{1}_m - \mathbf{b} \rangle \quad (31)$$

Applying the first-order optimality condition yields:

$$\frac{\partial \Phi(\boldsymbol{\pi}, \mathbf{f}, \mathbf{g})}{\partial \pi_{ij}} = \mathbf{D}_{ij} + \epsilon \log(\pi_{ij}) - \mathbf{f}_i - \mathbf{g}_j = 0, \quad (32)$$

Leading to an explicit formula for the optimal transport matrix $\boldsymbol{\pi}^\epsilon$:

$$\pi_{ij}^\epsilon = \exp\left(\frac{\mathbf{f}_i}{\epsilon}\right) \cdot \exp\left(-\frac{\mathbf{D}_{ij}}{\epsilon}\right) \cdot \exp\left(\frac{\mathbf{g}_j}{\epsilon}\right), \quad (33)$$

Defining $\mathbf{u}_i := \exp(\mathbf{f}_i/\epsilon)$, $\mathbf{v}_j := \exp(\mathbf{g}_j/\epsilon)$, and $\mathbf{K}_{ij} := \exp(-\mathbf{D}_{ij}/\epsilon)$, we can express $\boldsymbol{\pi}^\epsilon$ as $\text{diag}(\mathbf{u})\mathbf{K}\text{diag}(\mathbf{v})$. This transport matrix must satisfy the mass-preserving constraints:

$$\text{diag}(\mathbf{u})\mathbf{K}\text{diag}(\mathbf{v})\mathbf{1}_m = \mathbf{a}, \quad \text{diag}(\mathbf{v})\mathbf{K}^\top\text{diag}(\mathbf{u})\mathbf{1}_n = \mathbf{b}, \quad (34)$$

These constraints are equivalent to the matrix scaling problem, solvable iteratively as :

$$\mathbf{u}^{(\ell+1)} = \frac{\mathbf{a}}{\mathbf{K}\mathbf{v}^{(\ell)}}, \quad \mathbf{v}^{(\ell+1)} = \frac{\mathbf{b}}{\mathbf{K}^\top\mathbf{u}^{(\ell+1)}} \quad (35)$$

Thus, the Sinkhorn algorithm facilitates an efficient resolution to the entropy-regularized optimal transport problem, enabling the computation of the Sinkhorn discrepancy \mathbb{W}^ϵ as outlined in Equation (30).

B.3 Fused-gromov optimal transport and Frank-wolfe algorithm

While the Kantorovich problem effectively computes the discrepancy between discrete measures as in (4), it does not consider the local similarities within each measure which include fruitful geometric information. Incorporating local similarities can produce plausible transport strategy. An exemplar approach is the Gromov-Wasserstein measure, which generates transport matrix merely using the local similarities within each distribution. It has been primarily applied to matching objects with geometric structures [37, 63].

Definition B.3. *The Gromov-Wasserstein measure defines a cost-minimization task as follow*

$$\mathbb{G}(\alpha, \beta) := \min_{\boldsymbol{\pi} \in \Pi(\alpha, \beta)} \left(\sum_{i,j,k,l} \mathbf{P}_{i,j,k,l} \pi_{i,j} \pi_{k,l} \right) \quad (36)$$

where $\Pi(\alpha, \beta) := \{\boldsymbol{\pi} \in \mathbb{R}_+^{n \times m} : \boldsymbol{\pi} \mathbf{1}_m = \mathbf{a}, \boldsymbol{\pi}^\top \mathbf{1}_n = \mathbf{b}\}$ represents the set of feasible transport matrices, $\mathbb{G}(\alpha, \beta)$ represents the Gromov-Wasserstein discrepancy between α and β ; \mathbf{a}, \mathbf{b} are vectors describing the mass distribution in α and β , respectively. $\mathbf{P}_{i,j,k,l} = \|\mathbf{D}_{i,k}^{T=0} - \mathbf{D}_{j,l}^{T=1}\|$, where $\mathbf{D}_{i,j}^t = \|\mathcal{R}_{\psi,i}^{T=t} - \mathcal{R}_{\psi,j}^{T=t}\|_2^2$ denotes the distances between samples within each measure computed using the squared Euclidean metric [9].

The Gromov-Wasserstein measure, as stated in Definition B.3, depicts local similarity within each treatment group as $\mathbf{D}_{i,j}^t = \|\mathcal{R}_{\psi,i}^{T=t} - \mathcal{R}_{\psi,j}^{T=t}\|$, and preserve such local similarity via $\mathbf{P}_{i,j,k,l} = \|\mathbf{D}_{i,k}^{T=0} - \mathbf{D}_{j,l}^{T=1}\|$. Specifically, if the distance between $\mathcal{R}_{\psi,i}^{T=0}$ and $\mathcal{R}_{\psi,i}^{T=0}$ is close to that between $\mathcal{R}_{\psi,i}^{T=1}$ and $\mathcal{R}_{\psi,l}^{T=1}$ (i.e., $\|\mathbf{D}_{i,k}^{T=0} - \mathbf{D}_{j,l}^{T=1}\| \rightarrow 0$), a higher volume of mass will be matched, indicated by a larger $\pi_{i,j} \pi_{k,l}$. Conversely, if there is a significant disparity, less mass will be transported. The derived transport plan encourages matching units with similar neighbors, preserving local similarity.

To further enhance the model by integrating global distribution alignment with local similarity preservation, the Fused Gromov-Wasserstein (FGW) problem was constructed [53], combining the

Algorithm 2 The Frank-wolfe algorithm to solve the fused-gromov optimal transport problem.

Input: empirical distributions α and β with n and m samples, respectively.

Parameter: ℓ_{\max} : stopping threshold.

Output: \mathbb{F} : the optimum transportation cost.

- 1: $\ell \leftarrow 0$, $\boldsymbol{\pi}^\ell \leftarrow \mathbf{1}_n \mathbf{1}_m^\top / m * n$.
 - 2: **while** $\ell < \ell_{\max}$ **do**
 - 3: $\hat{\boldsymbol{\pi}} \leftarrow \arg \min_{\boldsymbol{\pi} \in \Pi(\alpha, \beta)} \langle \boldsymbol{\pi}, \nabla_{\boldsymbol{\pi}} F(\boldsymbol{\pi}^\ell, \alpha, \beta) \rangle$
 - 4: $\tilde{\boldsymbol{\pi}} \leftarrow \hat{\boldsymbol{\pi}} - \boldsymbol{\pi}^\ell$.
 - 5: $\delta^* \leftarrow \arg \min_{0 \leq \delta \leq 1} (\kappa \cdot \langle \boldsymbol{\pi}^\ell + \delta \tilde{\boldsymbol{\pi}}, \mathbf{D} \rangle + (1 - \kappa) \cdot \sum_{i,j,k,l} \mathbf{P}_{i,j,k,l} \mathbf{P}_{i,j,k,l} (\boldsymbol{\pi}^\ell + \delta \tilde{\boldsymbol{\pi}})_{i,j} (\boldsymbol{\pi}^\ell + \delta \tilde{\boldsymbol{\pi}})_{k,l})$.
 - 6: $\boldsymbol{\pi}^{\ell+1} \leftarrow \boldsymbol{\pi}^\ell + \delta^* \tilde{\boldsymbol{\pi}}$.
 - 7: $\ell \leftarrow \ell + 1$.
 - 8: $\boldsymbol{\pi}^* \leftarrow \boldsymbol{\pi}^\ell$, $\mathbb{F} \leftarrow (\kappa \cdot \langle \boldsymbol{\pi}^*, \mathbf{D} \rangle + (1 - \kappa) \cdot \sum_{i,j,k,l} \mathbf{P}_{i,j,k,l} \mathbf{P}_{i,j,k,l} \boldsymbol{\pi}_{i,j}^* \boldsymbol{\pi}_{k,l}^*)$.
-

traditional Wasserstein measure with the Gromov-Wasserstein measure as formulated in Definition B.4.

Definition B.4. The FGW problem seeks to minimize a combined transport cost:

$$\mathbb{F}(\alpha, \beta) := \min_{\boldsymbol{\pi} \in \Pi(\alpha, \beta)} \left(\kappa \cdot \langle \boldsymbol{\pi}, \mathbf{D} \rangle + (1 - \kappa) \cdot \sum_{i,j,k,l} \mathbf{P}_{i,j,k,l} \boldsymbol{\pi}_{i,j} \boldsymbol{\pi}_{k,l} \right), \quad (37)$$

where κ is a balancing coefficient between the traditional Wasserstein cost and the Gromov-Wasserstein cost, $\mathbb{F}(\alpha, \beta)$ represents the discrepancy between α and β .

The FGW problem encompasses two distinct components whose contributions are regulated by the coefficient κ . The first term follows the traditional Kantorovich formulation as detailed in Definition 2.4, addressing the global distribution discrepancies. The second term, rooted in the Gromov-Wasserstein formulation from Definition B.3, focuses on measuring and preserving local similarities within each measure. Consequently, the minimization of $\mathbb{F}(\alpha, \beta)$ simultaneously aligns the measures α and β while conservatively maintaining their inherent local structures.

The FGW problem is a quadratic optimization problem with linear constraints, which enables the application of Frank-wolfe algorithm, an algorithm well-suited for standard quadratic programming, to solve the problem. The choice of the Frank-Wolfe algorithm for solving FGW is motivated by two key factors. Firstly, the linearization trick is particularly advantageous for FGW since the constraints are linear, which reduces the sub-problem in each iteration to a standard linear programming problem that can be solved efficiently. Secondly, it circumvents the computational burden of projections onto the feasible set, which can be particularly demanding in large-scale scenarios.

The procedure for solving the FGW problem using the Frank-Wolfe algorithm is encapsulated in Algorithm 2. The initial step involves setting the transport matrix $\boldsymbol{\pi}^0$ to a uniform distribution across $\mathbf{1}_n \mathbf{1}_m^\top / (m \cdot n)$, ensuring all entries start within the feasible set Π . At each iteration k , the algorithm determines an optimal direction by minimizing a linear approximation of $\mathbb{F}(\cdot)$ at $\boldsymbol{\pi}^k$. After this, a line search is performed to establish the step size δ^k . The transport matrix is then updated accordingly. Upon reaching a predefined stopping criterion, the final transport plan $\boldsymbol{\pi}^*$ is used to compute the optimal cost as defined by $\mathbb{F}(\cdot)$ in (37).

B.4 Complexity Analysis

One primary concern would be the overall complexity of solving discrete optimal transport problems. In this section, we investigate the actual running time of the proposed method. Specifically, we delve into the complexity of solving the FGW problem with Algorithm 2. Our investigation focuses on the interplay between the batch size (N), the number of features (D), and the maximum iterations (ℓ_{\max}) in Algorithm 2. The experiments are conducted using Intel® Xeon® Gold 6140 CPUs and Nvidia RTX 4090 GPUs, and each test is repeated 100 times to ensure the reliability of the results. Results are presented in Figure 5 and delineated below.

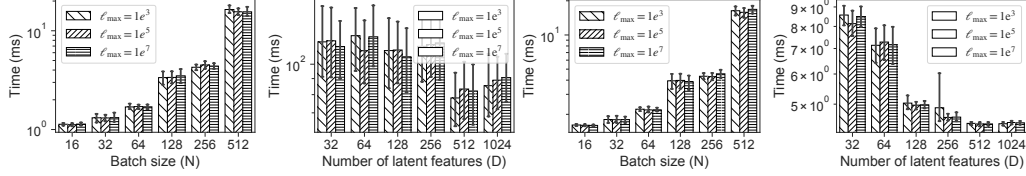


Figure 5: Running time of solving FGW using Algorithm 2 with different batch size (N) and feature number (D) on CPUs (a) and GPUs (b). Different patches represent various maximum iterations (ℓ_{\max}) used to solve the FGW problem. The error bars around these lines indicate the 99.9% confidence intervals.

- To examine the impact of batch size (N) on the running cost, we vary N from 16 to 512 while fixing the number of features (D) at 8. An increase in batch size (N) leads to a corresponding rise in the running cost, which aligns with expectations, as a larger batch size increases the scale of the transport matrix (π), which increases the scale of the optimization problem. Nevertheless, the escalation does not hinder the utility of FGW in a wide range, with the running time less than 1 second given a large batch size B=512.
- To examine the relationship between the number of features (D) and the running time, keep the batch size constant at 128. The results show a direct but modest positive correlation between D and running time. This can be explained by the influence of D on calculating the pairwise distance matrix (D) and the adjacency matrix (S). Although D affects these matrices, it does not significantly impact the scale of the transport matrix which is solely dependent on the batch size. Moreover, due to the curse of dimensionality, the distance between samples tend to be uniform given large D, which renders FGW earlier to converge to a trivial solution.
- There is a notable phenomenon regarding the running time under different ℓ_{\max} settings. The running time remains nearly identical for ℓ_{\max} values of $1e^5$ and $1e^7$ in specific configurations. This is likely due to the early convergence of the Frank-wolfe algorithm, which achieves convergence (characterized by little change of decision variables between two updates) before reaching the maximum iterations, resulting in similar running times for these ℓ_{\max} values.

C Reproduction details

C.1 Datasets

We conduct experiments on two semi-synthetic benchmarks to validate our models. For the IHDP³ benchmark, we report the results over 10 simulation realizations following [67]. However, the limited size (747 observations and 25 covariates) makes the results highly volatile. As such, we mainly validate the models on the ACIC benchmark, which was released by the ACIC-2016 competition⁴.

All datasets are randomly shuffled and partitioned in a 0.7:0.15:0.15 ratio for training, validation, and test, where we maintain the same ratio of treated units in all three splits to avoid numerical unreliability in the validation and test phases. We find that these datasets are overly easy to fit by the model because they are semi-synthetic. To increase the distinguishability of the results, we omit preprocessing strategies, such as min-max scaling, to increase the difficulty of the learning task.

C.2 Baselines

The collection of baselines involves statistical estimators [22, 49], matching estimators [10, 46, 55] and representation-based estimators [19, 49]. We implement these baselines based on Pytorch for neural network models, Sklearn for statistical models, and EconML for tree and forest models.

³It can be downloaded from <https://www.fredjio.com/>

⁴It can be downloaded from <https://jenniferhill7.wixsite.com/acic-2016/competition>

Table 3: In-sample performance (mean \pm std) on the ACIC and IHDP datasets. “*” marks the baseline estimators that NCR outperforms significantly at p-value < 0.05 over paired samples t-test.

Dataset	ACIC			IHDP		
	ϵ_{PEHE}	ϵ_{ATE}	ϵ_{ATT}	ϵ_{PEHE}	ϵ_{ATE}	ϵ_{ATT}
R.Forest	3.5946 \pm 0.0668*	0.3244 \pm 0.1358	0.4552 \pm 0.1648*	2.6356 \pm 3.5987	0.1365 \pm 0.1700	0.7952 \pm 1.9538
S.Learner	4.1777 \pm 0.3916*	1.6800 \pm 0.2529*	2.1471 \pm 0.7760*	5.3393 \pm 3.2868*	3.5985 \pm 2.9755*	2.5261 \pm 2.5642*
T.Learner	4.2147 \pm 0.4324*	1.7720 \pm 0.6134*	2.2644 \pm 0.7202*	1.4596 \pm 1.3833*	0.6004 \pm 1.2126	0.2138 \pm 0.3338
TARNet	3.4737 \pm 0.8818	1.1682 \pm 0.6491	1.5235 \pm 0.9131	0.6193 \pm 0.5409	0.1563 \pm 0.1435	0.2067 \pm 0.1753
k-NN	5.6057 \pm 0.1689*	1.5648 \pm 0.1365*	1.8345 \pm 0.1996*	2.2086 \pm 2.2338*	0.1402 \pm 0.2179	0.6570 \pm 1.3411
O.Forest	2.9224 \pm 0.2107	0.5827 \pm 0.1000	0.7417 \pm 0.1159	2.7186 \pm 2.6768*	0.4233 \pm 0.6500	0.1183 \pm 0.0957*
PSM	5.2301 \pm 0.1542*	0.2138 \pm 0.095	0.1699 \pm 0.1378*	3.2190 \pm 4.3526	0.2757 \pm 0.2024*	0.4201 \pm 0.6037
CFR-MMD	3.5946 \pm 0.2978*	1.3504 \pm 0.5154*	1.8273 \pm 0.6427*	0.9760 \pm 1.2489	0.5109 \pm 1.1672	0.3155 \pm 0.2419
CFR-WASS	3.4288 \pm 0.3952*	1.1796 \pm 0.6443*	1.9186 \pm 0.8632*	0.9008 \pm 1.2854	0.4802 \pm 1.1735	0.2353 \pm 0.2248
SITE	3.9685 \pm 0.7197*	1.2545 \pm 0.5110*	1.4734 \pm 0.5480	0.5922 \pm 0.5468	0.1323 \pm 0.1429	0.2099 \pm 0.2363
DESCN	2.6722 \pm 0.4088	0.0967 \pm 0.0674*	0.1419 \pm 0.1129*	3.8255 \pm 4.8384*	1.9369 \pm 3.0778	0.8617 \pm 2.4105
ESCFR	3.0362 \pm 0.6272	1.0632 \pm 0.5245*	1.6404 \pm 0.8427	0.5824 \pm 0.4628	0.1172 \pm 0.1191	0.2330 \pm 0.2115
NCR	2.6091 \pm 0.7673	0.5384 \pm 0.3932	1.0313 \pm 0.7206	0.4439 \pm 0.2453	0.1158 \pm 0.1022	0.2922 \pm 0.2464

Table 4: Performance (mean \pm std) on the outcome regression metrics. “*” marks the baseline estimators that NCR outperforms significantly at p-value < 0.05 over paired samples t-test.

Dataset	ACIC				IHDP			
	R_F^2	R_{CF}^2	RMSE _F	RMSE _{CF}	R_F^2	R_{CF}^2	RMSE _F	RMSE _{CF}
R.Forest	0.6467 \pm 0.0555*	0.4888 \pm 0.0655*	3.4986 \pm 0.245*	3.5238 \pm 0.2581*	0.7601 \pm 0.1764*	0.7015 \pm 0.3569	3.7869 \pm 7.2249	2.3231 \pm 4.1016
S.Learner	0.4639 \pm 0.2501*	0.2667 \pm 0.1795*	4.1216 \pm 0.9700*	4.4058 \pm 0.5470*	-2.7879 \pm 4.2168*	-11.2793 \pm 13.0602*	4.6996 \pm 3.4374*	5.4704 \pm 3.2770*
T.Learner	0.5290 \pm 0.1005*	0.2806 \pm 0.1195*	3.9372 \pm 0.4287*	4.3787 \pm 0.3865*	0.6952 \pm 0.7542	-0.0314 \pm 2.6107	1.8941 \pm 3.1344	1.5704 \pm 1.3631*
TARNet	0.6662 \pm 0.2041	0.4942 \pm 0.2699	3.2011 \pm 0.9756	3.5595 \pm 1.0028	0.9550 \pm 0.0111	0.9566 \pm 0.0301*	1.3934 \pm 2.5739	0.5007 \pm 0.285
k-NN	0.2687 \pm 0.0764*	-0.2455 \pm 0.1093*	5.0454 \pm 0.2777*	5.5067 \pm 0.2843*	0.6635 \pm 0.1068*	0.6787 \pm 0.1395*	3.8669 \pm 6.8299	2.0649 \pm 2.7581
O.Forest	-	-	-	-	-	-	-	-
PSM	0.7110 \pm 0.0218	-0.0665 \pm 0.1209*	3.1795 \pm 0.2533*	5.0937 \pm 0.3254*	0.7539 \pm 0.1371*	0.2789 \pm 0.9195*	3.3523 \pm 5.6795	3.5286 \pm 6.4727
CFR-MMD	0.6966 \pm 0.0498*	0.5278 \pm 0.0917*	3.1674 \pm 0.2542*	3.5455 \pm 0.3359*	0.7601 \pm 0.6152	0.1906 \pm 2.3232	1.6235 \pm 2.7575	1.0193 \pm 1.2497
CFR-WASS	0.7276 \pm 0.0394	0.5562 \pm 0.0884*	3.0027 \pm 0.2226*	3.435 \pm 0.3516*	0.7652 \pm 0.6169	0.2163 \pm 2.3319	1.6341 \pm 2.7939	0.9951 \pm 1.2898
SITE	0.4979 \pm 0.1915*	0.3317 \pm 0.2329*	4.0082 \pm 0.8403*	4.1632 \pm 0.8184*	0.9271 \pm 0.0294*	0.9442 \pm 0.0317*	1.6782 \pm 3.1058	0.6867 \pm 0.6654
DESCN	0.7911 \pm 0.0624	0.6465 \pm 0.1293	2.6130 \pm 0.3684	3.0384 \pm 0.5320	-0.3414 \pm 3.6949	-3.2670 \pm 11.6581	3.2771 \pm 5.0446	3.5789 \pm 4.5460
ESCFR	0.7500 \pm 0.1262	0.6221 \pm 0.1655	2.8063 \pm 0.7001	3.1153 \pm 0.6960	0.9423 \pm 0.0284	0.9397 \pm 0.0427	1.5723 \pm 2.9793	0.6283 \pm 0.5031
NCR	0.8131 \pm 0.1718	0.7292 \pm 0.2285	2.3478 \pm 0.8852	2.5482 \pm 0.9279	0.9550 \pm 0.0111	0.9566 \pm 0.0301	1.3934 \pm 2.5739	0.5007 \pm 0.2850

D Complementary Results

We provide In-sample results in Table 3 and detailed regression metrics for factual and counterfactual outcomes in Table 4.